

Characterization of shift-variant pupil aberrations for wide field-of-view microscopy

Guoan Zheng,^{*,†} Xiaoze Ou,[†] Roarke Horstmeyer, and Changhui Yang

Department of Electrical Engineering, California Institute of Technology, Pasadena, CA 91125, USA

[†]*These authors contributed equally to this work*

Correspondence: gazheng@caltech.edu

Abstract: We describe a simple and robust approach for characterizing the shift-variant pupil aberrations of wide field-of-view microscopy systems. We derive the microscope's location-dependent pupil transfer functions by first capturing multiple intensity images at different defocus settings; a generalized pattern search (GPS) algorithm is then applied to recover the complex pupil functions at ~350 different spatial locations over the entire field-of-view. Parameter fitting transforms these pupil functions into accurate 2D aberration maps. We demonstrate shift-variant aberration compensation by using an information-preserving image deconvolution scheme over the entire field-of-view. Such automated shift-variant pupil characterization will facilitate new approaches of aberration correction for future gigapixel imaging platforms.

OCIS codes: (170.0180) Microscopy; (100.0100) Image processing

References and links

1. O. S. Cossairt, D. Miao, and S. K. Nayar, "Scaling law for computational imaging using spherical optics," *JOSA A* 28, 2540-2553 (2011).
2. D. Brady, M. Gehm, R. Stack, D. Marks, D. Kittle, D. Golish, E. Vera, and S. Feller, "Multiscale gigapixel photography," *Nature* 486, 386-389 (2012).
3. F. Bery and S. Slansky, "Wavefront determination resulting from Foucault test as applied to the human eye and visual instruments," *Optical instruments and techniques*, 375-386 (1969).
4. S. Yokozeki and K. Ohnishi, "Spherical aberration measurement with shearing interferometer using Fourier imaging and moiré method," *Applied optics* 14, 623-627 (1975).
5. M. Ma, X. Wang, and F. Wang, "Aberration measurement of projection optics in lithographic tools based on two-beam interference theory," *Applied optics* 45, 8200-8208 (2006).
6. M. Takeda and S. Kobayashi, "Lateral aberration measurements with a digital Talbot interferometer," *Applied Optics* 23, 1760-1764 (1984).
7. J. Sung, M. Pitchumani, and E. G. Johnson, "Aberration measurement of photolithographic lenses by use of hybrid diffractive photomasks," *Applied optics* 42, 1987-1995 (2003).
8. Q. Gong and S. S. Hsu, "Aberration measurement using axial intensity," *Optical Engineering* 33, 1176-1186 (1994).
9. L. N. Thibos, "Principles of hartmann-shack aberrometry," in *Vision Science and its Applications*, (Optical Society of America, 2000),
10. J. Beverage, R. Shack, and M. Descour, "Measurement of the three - dimensional microscope point spread function using a Shack - Hartmann wavefront sensor," *Journal of microscopy* 205, 61-75 (2002).
11. L. Seifert, J. Liesener, and H. J. Tiziani, "The adaptive Shack-Hartmann sensor," *Optics Communications* 216, 313-319 (2003).
12. R. Lane and M. Tallon, "Wave-front reconstruction using a Shack-Hartmann sensor," *Applied optics* 31, 6902-6908 (1992).
13. R. G. Paxman, T. J. Schulz, and J. R. Fienup, "Joint estimation of object and aberrations by using phase diversity," *JOSA A* 9, 1072-1085 (1992).
14. B. M. Hanser, M. G. Gustafsson, D. A. Agard, and J. W. Sedat, "Phase retrieval for high-numerical-aperture optical systems," *Optics letters* 28, 801-803 (2003).
15. B. Hanser, M. Gustafsson, D. Agard, and J. Sedat, "Phase - retrieved pupil functions in wide - field fluorescence microscopy," *Journal of microscopy* 216, 32-48 (2004).

16. J. R. Fienup, "Phase-retrieval algorithms for a complicated optical system," *Applied optics* 32, 1737-1746 (1993).
 17. J. Fienup, J. Marron, T. Schulz, and J. Seldin, "Hubble Space Telescope characterized by using phase-retrieval algorithms," *Applied optics* 32, 1747-1767 (1993).
 18. G. R. Brady and J. R. Fienup, "Nonlinear optimization algorithm for retrieving the full complex pupil function," *Opt. Express* 14, 474-486 (2006).
 19. Y. Kawano, C. Higgins, Y. Yamamoto, J. Nyhus, A. Bernard, H.-W. Dong, H. J. Karten, and T. Schilling, "Darkfield Adapter for Whole Slide Imaging: Adapting a Darkfield Internal Reflection Illumination System to Extend WSI Applications," *PLOS ONE* 8, e58344 (2013).
 20. C. Audet and J. E. Dennis Jr, "Analysis of generalized pattern searches," *SIAM Journal on Optimization* 13, 889-903 (2002).
 21. A. W. Lohmann, R. G. Dorsch, D. Mendlovic, Z. Zalevsky, and C. Ferreira, "Space-bandwidth product of optical signals and systems," *JOSA A* 13, 470-473 (1996).
 22. H. Gross, W. Singer, M. Totzeck, F. Blechinger, and B. Ahtner, *Handbook of optical systems* (Wiley Online Library, 2005), Vol. 2.
 23. X. Yang, H. Li, and X. Zhou, "Nuclei segmentation using marker-controlled watershed, tracking using mean-shift, and kalman filter in time-lapse microscopy," *Circuits and Systems I: Regular Papers, IEEE Transactions on* 53, 2405-2414 (2006).
 24. B. K. Gunturk and X. Li, *Image Restoration: Fundamentals and Advances* (CRC Press, 2012), Vol. 7.
 25. T. McReynolds and D. Blythe, *Advanced graphics programming using OpenGL* (Morgan Kaufmann, 2005).
 26. J. W. Goodman, *Introduction to Fourier optics* (Roberts & Company Publishers, 2005).
-

1. Introduction

The characterization of optical system aberrations is critical in applications such as ophthalmology, microscopy, photolithography, and optical testing. Knowledge of the aberrations in these different imaging platforms affords their correction through either adaptive optics or post-detection image deconvolution, leading to improved system performance and reproducibility. Such digital aberration removal techniques may also lead to simple and compact gigapixel imaging systems exhibiting a high resolution over a wide field-of-view (FOV) [1, 2]. Here, we describe an automated aberration identification pipeline amenable to the quick and robust calibration of such computation-based wide FOV imaging designs.

In the past 40 years, many unique wavefront sensing methods have been proposed for aberration measurement [3-12]. The most notable methods utilize a Shack-Hartmann wavefront sensor [9-11], which consists of an array of microlenses of the same focal length that each focus light onto a detector. The local tilt of an incident wavefront across one microlens can be calculated from the position of its detected focal spot. Using the local tilts computed for the entire microlens array, the amplitude and phase of the incident wavefront can be directly approximated. Despite offering high accuracy, the Shack-Hartmann sensor often requires considerable modification to an existing optical setup. For example, as the wavefront sensor needs to be placed at the pupil plane of the imaging platform, additional relay lenses may be required that are each subject to possible misalignment.

Alternatively, wavefront aberrations can be inferred directly from intensity measurements by relying upon phase retrieval strategies [13-18]. A common phase retrieval-based strategy is to introduce phase diversity [13, 18] between multiple measurements of the intensity of an aberrated optical field. Examples of phase diversity include the addition of optical elements or introducing system defocus. Such defocus diversity (i.e., capturing multiple intensity images of the sample with known sensor displacements) can successfully recover the complex pupil function of a high numerical aperture (NA) microscope objective lens [14, 15, 18]. However, for simplicity, these previous approaches assumed the aberrated objective lens is independent of the image plane's spatial coordinates [13-15, 18]. This approximation of a shift-invariant point-spread-function (PSF) only remains valid for objective lenses exhibiting a very small FOV. Off-axis aberrations must be considered in wide FOV systems, like those targeted for computation-based gigapixel photography [1, 2] and whole slide imaging [19], as the microscope's aberrated PSF varies significantly in shape across the image plane.

In this paper, we describe a phase retrieval approach to characterize such shift-variant wavefront aberrations of wide FOV microscopy platforms. We apply a generalized pattern search (GPS) optimization algorithm [20] to recover aberration parameters at ~ 350 different spatial locations over the entire FOV. These parameters are then used to generate 2D aberration maps by parameter fitting. Based upon the recovered aberration maps, we also perform post-detection shift-variant image deconvolution to compensate for wavefront aberrations over the entire FOV.

The remainder of this paper is structured as follows: in Section 2, we describe the procedure of aberrated pupil function recovery at one location off the optical axis. In Section 3, we experimentally demonstrate how shift-variant aberrations may be automatically characterized over an entire imaging FOV. In Section 4, we report on a simple scheme for shift-variant image deconvolution to compensate for any measured system aberrations. Finally, we will discuss some advantages and limitations of the proposed pipeline.

2. Off-axis pupil function recovery

We use a conventional upright microscope (BX 41, Olympus) and a full-frame CCD camera (KAI-29050, Kodak) as our experimental setup. The objective lens under testing is a 2X apochromatic lens (0.08 NA, Olympus) with a relatively large FOV (~ 1.35 cm in diameter). Such a large FOV has the potential to facilitate whole slide imaging for different applications [19]. However, scale-dependent geometric aberrations compound any attempts to directly image this large FOV at high resolution [21]. Furthermore, these aberrations are shift-variant: aberrations are well-corrected near the optical axis, but second-order aberrations deteriorate image quality at the edge of the FOV.

Our goal here is to characterize (Sections 2 and 3) and digitally correct (Section 4) for such shift-variant aberrations. The proposed approach for off-axis aberration characterization consists of three primary steps: 1) sample preparation, 2) phase retrieval, and 3) pupil function estimation, as detailed below.

1) *Sample preparation.* We first create a calibration target by spin-coating a layer of 10-micron microspheres (Polysciences Inc.) on top of a microscope slide. We then use the upright microscope with the 2X objective lens to image this calibration target. We select a sparse concentration of microspheres to ensure that an automated search algorithm may successfully identify each microsphere. For example, we find that spreading approximately 350 microspheres randomly over the 2X objective's entire FOV (1.35 cm in diameter) works well.

2) *Phase retrieval.* We displace the microscope stage from the focal plane at $\delta = 50$ μm increments, capturing $s = 8$ images of the microsphere calibration target I_s in either defocus direction. A total of $2s + 1 = 17$ images are captured, with a maximum defocus distance $|s| \cdot \delta = 400$ μm . For each image, the target is illuminated with a quasi-monochromatic collimated plane wave (632 nm). We recover the complex profile of one microsphere selected at the center FOV of each image using a conventional multi-plane phase retrieval algorithm [13, 16]. Briefly, multi-plane phase retrieval operates as follows. First, the algorithm is initialized with an estimate of the complex field at the object plane. This initial estimate's phase is set to a constant and its amplitude is set to the square root of the first intensity measurement, I_0 . Second, this complex field estimate is Fourier transformed and multiplied by a quadratic phase factor, $e^{ik_z(k_x, k_y)z}$, describing defocus of the field by axial distance $z = s \cdot \delta$. To begin, we set $s = 1$, corresponding to $+50$ μm of defocus. By stepping through 17 values of s , we digitally propagate the complex field estimate to each position where a defocused image was captured. Third, after digitally defocusing, we again replace the amplitude values of the complex field estimate with the square root of the intensity data from recorded image I_s . Beginning with $s = 1$, we use the intensity values captured at $+50$ μm for amplitude value replacement, while the estimate's phase values remain unchanged. This propagate-and-replace process is repeated for all 17 intensity measurements in the captured focal stack. Finally, the

entire phase retrieval process is iterated approximately 10 times. The final recovered complex image, denoted as $\sqrt{I_{truth}} e^{i\phi_{truth}}$, serves as a microsphere's "ground truth" complex field, which may be digitally refocused to any position of interest.

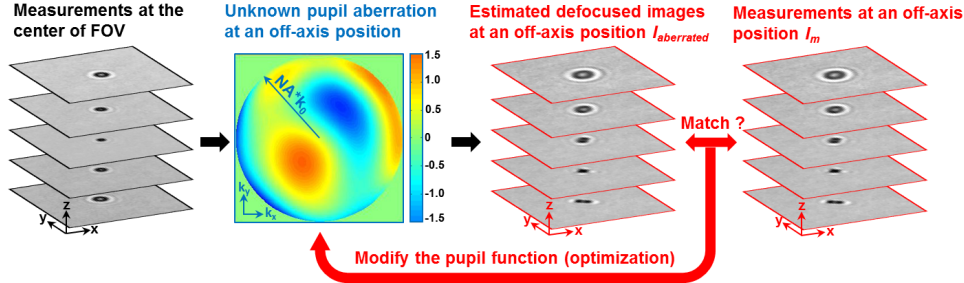


Fig. 1. Pupil function recovery at one off-axis position. Two cropped areas of one set of defocused intensity images are used for algorithm input. One cropped set $I_c(s)$ is centered on a microsphere at the images' central FOV (left), while the other cropped set $I_m(s)$ is centered on a microsphere at an off-axis position (right). Each cropped image set contains $s = 17$ intensity measurements (here only 5 are shown) at different defocus distances (-400 μm to +400 μm , 50 μm per step). We approximate an unknown pupil function W with 5 Zernike coefficients (x-tilt, y-tilt, x-astigmatism, y-astigmatism, and defocus). We use this pupil function estimate to modify the 17 "ground truth" images of the central microsphere $I_c(s)$ to generate a new set of aberrated intensity images, $I_{aberrated}(s)$. We then adjust the values of the 5 unknown Zernike coefficients to minimize the difference between $I_{aberrated}(s)$ and the actual intensity measurements of the off-axis microsphere, $I_m(s)$ (right). The corresponding pupil function described by 5 Zernike coefficients is recovered when the mean-squared error difference between these two sets of images is minimized.

3) *Off-axis pupil function estimation.* We next choose a microsphere at an off-axis position (x_0, y_0) and initialize an estimate of the unknown location-dependent pupil function $W(k_x, k_y, x_0, y_0)$. Here, k_x and k_y are wave numbers in the x and y directions. We approximate the unknown pupil function $W(k_x, k_y, x_0, y_0)$ with 5 Zernike modes, Z_1^{-1} , Z_1^1 , Z_2^{-2} , Z_2^2 , and Z_2^0 , corresponding to x -tilt, y -tilt, x -astigmatism, y -astigmatism, and defocus aberration, respectively [22]. The point-spread function at the chosen off-axis microsphere location (x_0, y_0) may be uniquely influenced by each mode above. We denote the coefficient for each Zernike mode with $p_m(x_0, y_0)$, where the subscript 'm' stands for the mode's polynomial expansion order (in our case, $m=1, 2, \dots, 5$). With this notation, our unknown pupil function estimate $W(k_x, k_y, x_0, y_0)$ can be expressed as,

$$W(k_x, k_y, x_0, y_0) = \exp[p_1(x_0, y_0)Z_1^{-1}(k_x, k_y) + p_2(x_0, y_0)Z_1^1(k_x, k_y) + \dots + p_3(x_0, y_0)Z_2^{-2}(k_x, k_y) + p_4(x_0, y_0)Z_2^2(k_x, k_y) + p_5(x_0, y_0)Z_2^0(k_x, k_y)] \quad (1)$$

Here, $p_m(x_0, y_0)$ is a space-dependent function evaluated at $(x = x_0, y = y_0)$, allowing the pupil function W to model shift-variant aberrations. This pupil function estimate is then used along with the recovered "ground truth" complex image of the central microsphere to generate a set of aberrated intensity images, $I_{aberrated}$, as follows:

$$I_{aberrated}(k) = |\mathcal{F}^{-1}(W(k_x, k_y, x_0, y_0) \times \mathcal{F}(\sqrt{I_{truth}} e^{i\phi_{truth}}))|^2, \quad (2)$$

where \mathcal{F} is the Fourier transform operator and the term $e^{i\phi_{truth}}$ represents defocus of the ground truth microsphere field to plane s . We then adjust the values of the 5 unknown Zernike coefficients p_m ($m=1, 2, \dots, 5$) describing the pupil function W to minimize the difference between this set of aberrated intensity images $I_{aberrated}$ and the actual intensity measurements of the selected off-axis microsphere, $I_m(s)$. The corresponding pupil function described by 5 Zernike coefficients is recovered when the mean-squared error difference is minimized. We

apply a GPS algorithm [20] to solve the following nonlinear optimization problem for pupil function recovery:

$$(p_1, p_2 \dots p_5) \Big|_{(x=x_0, y=y_0)} = \underset{(p_1, p_2 \dots p_5)}{\operatorname{argmin}} \sum_{17 \text{ images}} (\sqrt{I_{\text{aberrated}}} - \sqrt{I_m})^2 \quad (3)$$

Based on these optimal Zernike coefficients, the off-axis pupil function can be approximated following Eq. (1). Determining the aberration function associated with one off-axis microsphere requires an approximate computation time of 15 seconds on an Intel i7 CPU. This optimization process may directly extend to account for higher-order aberrations, with approximately 3x more computational time for one additional Zernike mode.

3. Shift-variant aberration characterization over the entire FOV

Repeating the previous section's off-axis aberration recovery scheme for many different microspheres, we can characterize the shift-variant aberrations of the microscope objective over its entire FOV. The microspheres are automatically identified following the marker-controlled watershed segmentation algorithm [23]. Distance between each marked microsphere and its nearest neighbor is examined and those microspheres with distances shorter than 150 μm are automatically unmarked to screen out microsphere clusters. Fig. 2(a) shows a full FOV image of the calibration target with ~ 350 microspheres denoted by a red dot. For each microsphere, we recover 5 location-specific Zernike coefficients. For example, Fig. 2(b) shows the pupil function W recovered following Eq. (2) at position 1, enclosed by the black square in Fig. 2(a). Fig. 2(c1)-(c5) are 5 of the 17 intensity measurements of the microsphere at position 1 under different amounts of defocus: $I_m(s=0)$, $I_m(s=\pm 3)$, and $I_m(s=\pm 6)$. Fig. 2(d1)-(d5) display the corresponding aberrated image estimates $I_{\text{aberrated}}(s)$ generated by the recovered pupil function in Fig. 2(b). Following the convex form of Eq. (2), the applied GPS algorithm successfully minimizes the mean-squared error difference between the measurements $I_m(s)$ and the estimates $I_{\text{aberrated}}(s)$.

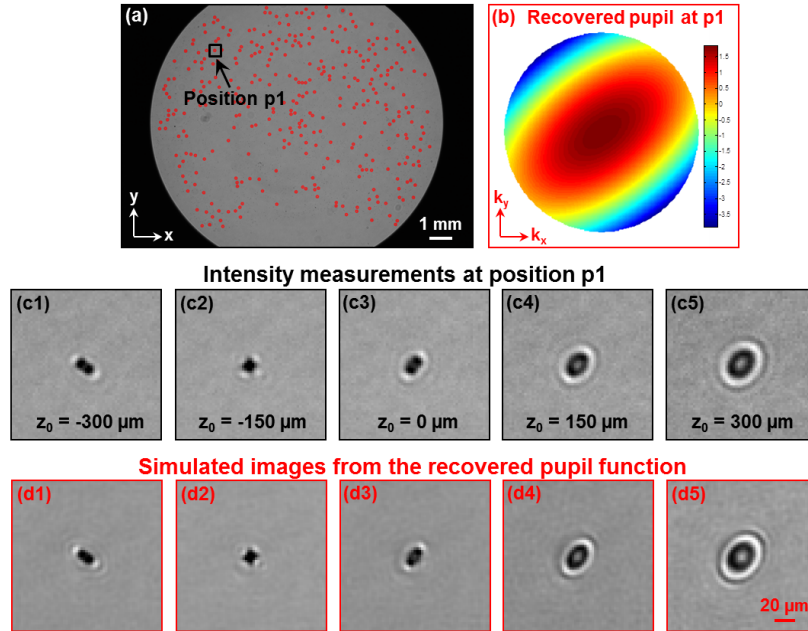


Fig. 2. Off-axis aberration characterization with a calibration target. (a) ~ 350 microspheres are automatically identified on a microscope slide, each denoted by a red dot. (b) The recovered pupil function at position 1. (c1)-(c5) Intensity measurements I_m of the microsphere at position 1 under different amounts of defocus. (d1)-(d5) The corresponding aberrated image estimates generated using the pupil function in Fig. 2(b).

The aberration recovery process is repeated for all microspheres at different locations within the calibration target. Thus, 5 Zernike coefficients are found for approximately 350 unique spatial locations over the entire FOV. Fig. 3(a)-(c) demonstrate the recovered second-order shift-variant aberrations of the 2X objective lens, corresponding to x-astigmatism, y-astigmatism, and defocus aberration respectively (first order Zernike modes are normally not considered as aberrations). The full FOV image of our calibration target is shown at the bottom plane ($p_m = 0$ plane) of each plot in Fig. 3, where the FOV diameter is about 1.35 cm. Each blue dot in Fig. 3 represents the recovered coefficient for the corresponding Zernike mode, and the spatial location of each blue dot corresponds to one microsphere labeled in Fig. 2(a). Finally, we fit these 350 values to a continuous polynomial function $p_m(x, y)$ across the spatial coordinates of the image plane. The results of such a fitting process are the curved surfaces shown Fig. 3. These fitted curves allow us to accurately recover the pupil function at any image plane location (x, y) .

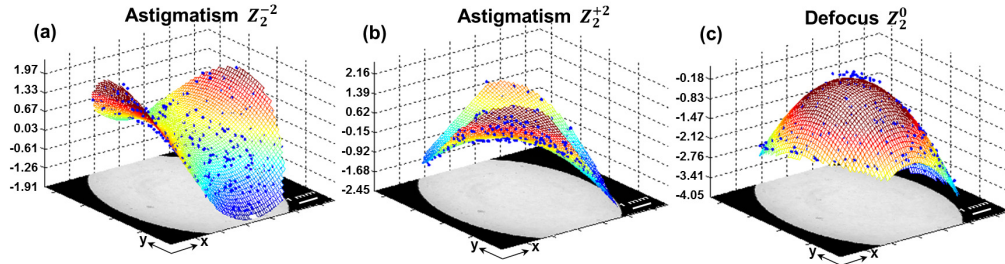


Fig. 3 Shift-variant aberrations of the 2X objective lens. Each data point, denoted by a blue dot, represents the extracted Zernike coefficient weight for one microsphere. ~ 350 microspheres are identified over the entire FOV and their corresponding parameters are fitted to a 2D surface for each type of aberration. (a)-(c) correspond to x-astigmatism, y-astigmatism and defocus.

An additional experiment was performed to verify the accuracy of our aberration parameter recovery. We defocused the calibration target by $+50$ microns along the optical axis and again implemented our aberration parameter recovery process (using the same ground truth images as before). Fig. 4 shows the defocus parameter with and without $+50$ μm of sample defocus. According to aberration theory, the two interpolated surfaces can be expressed as a second order polynomial function [22], $z(x, y) = t_{00} + t_{10}x + t_{01}y + t_{20}x^2 + t_{11}xy + t_{02}y^2$. The major difference between these two surfaces is the t_{00} parameter, and the difference corresponds to 48.9 μm , which is in a good agreement of the actual $+50$ μm defocus distance.

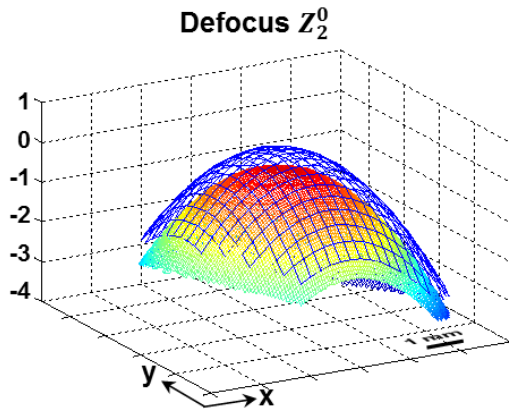


Fig. 4 Recovered defocus parameters with (color surface) and without (blue grid) $+50$ μm of sample defocus. The difference between these two surfaces corresponds to a defocus distance of $+48.9$ μm , which is in a good agreement with the actual displacement distance.

4. Shift-variant image deconvolution

To demonstrate the utility of our proposed aberration characterization pipeline, we perform shift-variant image deconvolution over the entire FOV of microscope objective. The shift-variant image deconvolution process is comprised of three main steps: 1) phase retrieval, 2) segment decomposition and shift-invariant image deconvolution, and 3) image segment recombination, as outlined below.

1) *Phase retrieval of the full-FOV image.* We use the multi-plane phase retrieval algorithm to recover a complex description (i.e., the amplitude and phase) of a sample over the microscope's entire FOV. This complex map contains the shift-variant aberrations of the objective lens.

2) *Segment decomposition and shift-invariant image deconvolution.* We divide the full-FOV complex image into smaller 128×128 pixel image segments, denoted by $I_{\text{seg}}(n)$ ($n = 1, 2, \dots, \mathbf{X}$ for our employed detector). Aberrations within each small segment are treated as shift-invariant, a common strategy for wide FOV imaging processing [24]. The pupil function $W(k_x, k_y, x_c(n), y_c(n))$ is then calculated for each small segment following Eq. (1), where $(x_c(n), y_c(n))$ represents the central spatial location of the n^{th} segment. We then perform image deconvolution to recover the corrected image segment $I_{\text{cor}}(n)$ as follows:

$$I_{\text{cor}}(n) = \left| \mathcal{F}^{-1} \left(\mathcal{F} \left(\sqrt{I_{\text{seg}}} e^{i\phi_{\text{seg}}} \right) / W(k_x, k_y, x_c(n), y_c(n)) \right) \right|^2 \quad (4)$$

We note that, in the above equation, we only perform division within the circular pupil of the objective lens; for regions outside the circular pupil, we set the spectrum to 0 in the Fourier domain. By using this scheme, we avoid dividing by zero in the Fourier domain.

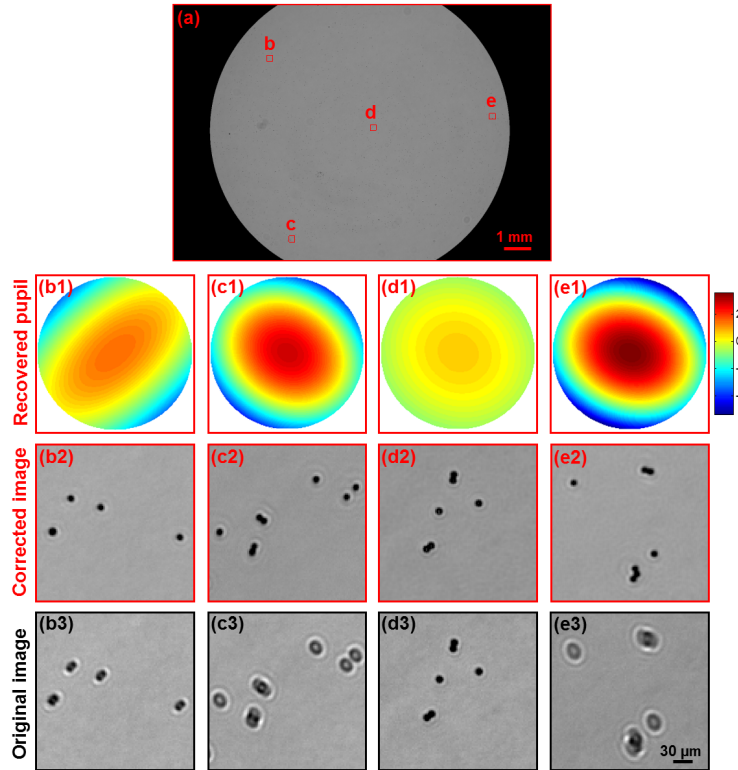


Fig. 5 Shift-variant image deconvolution using the calibration target. (a) The aberration-corrected full FOV image. (b1)-(e1) Recovered pupil functions corresponding to highlighted regions in (a). (b2)-(e2) The corrected images of highlighted regions in (a). (b3)-(e3) The original images of the test target without aberration correction.

3) *Image segment recombination*. In this final step, we recombine all the corrected image segments $I_{\text{cor}}(n)$ to form a correct full FOV image. An alpha blending algorithm [25] is used to remove edge artifacts during the recombination process. Specifically, we cut away 2 pixels at the edge of each segment and use another 5 pixels to overlap with the adjacent portions. This blending comes at a small computational cost of redundantly processing the regions of overlap twice.

Based on the image deconvolution process discussed above, Fig. 5 and Fig. 6 show the corrected full-FOV images of two samples. The first sample is the calibration target discussed in section 2, and the second sample is a new test target with a mixture of microspheres of different diameters (5-20 μm) on a microscope slide. The 4 regions highlighted by red squares in Fig. 5(a) and Fig. 6(a) are selected for detailed observation. The corresponding pupil functions of these four regions are shown in Fig. 5(b1)-(e1) and Fig. 6(b1)-(e1). Fig. 5(b2)-(e2) and Fig. 6(b2)-(e2) display their associated corrected (i.e., deconvolved) images, while Fig. 5(b3)-(e3) and Fig. 6(b3)-(e3) display their original images without aberration correction. From these two examples, we can see that the shift-variant aberrations of the objective lens can be digitally compensated for based on our aberration characterization procedures.

Finally, we note that, the above deconvolution scheme is based on inverting the coherent transfer function (the complex pupil function) of the objective lens in Eq. (4). For the case of incoherent illumination, the incoherent optical transfer function can be directly calculated from the complex pupil function through a close form equation [26], and image deconvolution can be performed in the Fourier domain accordingly.

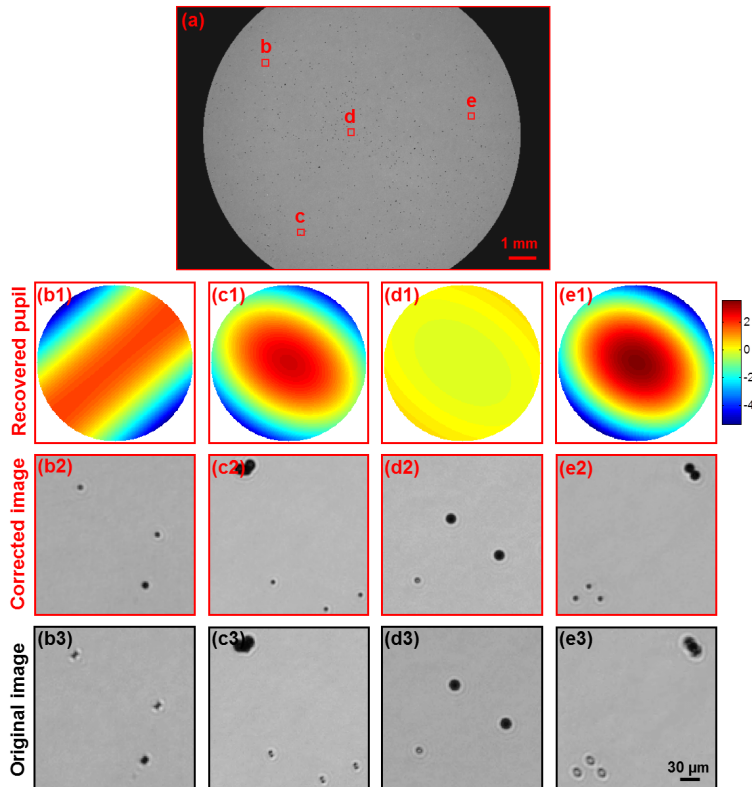


Fig. 6 Shift-variant image deconvolution using a new test target (a mixture of 5-20 micron microspheres). (a) The aberration-corrected full FOV image. (b1)-(e1) Recovered pupil functions corresponding to highlighted regions in (a). (b2)-(e2) The corrected images of highlight regions in (a). (b3)-(e3) The original images of the test target without aberration correction.

5. Conclusion

In summary, we report a phase retrieval-based procedure to efficiently recover the shift-variant wavefront aberrations common in wide-FOV microscope systems. We applied the generalized pattern search (GPS) algorithm to recover pupil functions at ~ 350 off-axis positions. These pupil functions were then used to generate 2D aberration maps by parameter fitting. We demonstrated the application of our characterization process with an example of shift-variant image deconvolution, which successfully accounts for induced aberrations over an entire FOV of a 2x objective (1.35cm diameter). The proposed computational approach does not require any optical modifications or additional hardware. The entire aberration recovery process is fully automated and easy to implement. We believe the characterization of shift-variant pupil aberrations is an attractive way to quantify the performance of many wide FOV image platforms and promises to play a major role in the future development of gigapixel imaging platforms.

Finally, we note that, the proposed characterization approach is currently used for 5 Zernike modes recovery. For more complicated imaging designs, 7-10 Zernike modes are needed for aberration characterization and a GPU will be useful for significantly shorting the associated processing time. On the other hand, we assume 100% transmission of objective lens at the back aperture plane. Modeling non-perfect transmission of the objective lens within our characterization framework will be another research direction in the future.

Acknowledgements

We acknowledge funding support from National Institute of Health under Grant No. 1R01AI096226-01.